

with  $m_{O_2}$  as the mass of the oxygen molecule. Thus, assuming a sticking coefficient of one for the oxygen molecules and recognising that each hit of an  $O_2$  molecule results in 2 oxygen atoms sticking to the surface, the maximal layer-growth rate is given by  $2 \cdot z \cdot V_{ox}$ , with  $V_{ox}$  being the volume of oxide formed per oxygen atom. If MgO, with  $V_{ox} = 0.0187 \text{ nm}^3$ , would be formed at 302 K, the maximum oxidation rate would be 0.133 nm/L. The experimentally observed layer-growth rate is much larger up to a thickness of about 1 nm (see Fig. 4.13), which implies that  $V_{ox}$  must be considerably larger than that of MgO and consequently the concentration of oxygen in the oxide layer is distinctly smaller than that of MgO. The initial oxidation rate of the actually developing oxide is  $\sim 1.1 \text{ nm/L}$  for oxygen exposures  $< 1 \text{ L}$  corresponding to  $V_{ox} = 0.155 \text{ nm}^3$  which corresponds to an oxygen density of about  $11 \text{ mol/dm}^3$ .

Furthermore, comparison of HERDA measurements of the oxygen intensity of a pure MgO single crystal and of an oxidised Mg specimen also revealed a pronounced oxygen deficiency in the oxide grown on Mg, also even at the surface confirming the above discussed XPS results; see Figs. 4.11 and 4.12. Two examples of HERDA oxygen spectra measured after oxidation for different oxygen exposures are shown in Fig. 4.14, together with the O intensity level measured for the MgO single crystal: The maximum oxygen intensity of the oxidised Mg sample is only  $\sim 50 \%$  of that of the MgO standard sample.

The HERDA measurements showed that upon increasing oxygen exposure the oxygen deficiency decreased (Fig. 4.15), which tendency also agrees with the XPS data shown in Fig. 4.12.

The HERDA measurement of a Mg sample covered with the *native* oxide showed a maximum peak height equal to that of the MgO standard, indicating the existence of stoichiometric MgO for the native layer. Thus, despite of an oxide layer thickness similar to that of the specimen oxidised in UHV, the composition of both oxides is very different indicating a strong difference between initial and very late stages of oxide development.

A large Mg/O ratio for the initial oxidation stage could be due to a small number of oxygen ions ionising a large number of Mg atoms. This is actually predicted in the theoretical work of Ref. [45], where it is shown that oxygen always has a valence state of -2, almost independent of the local co-ordination, whereas the surrounding Mg atoms

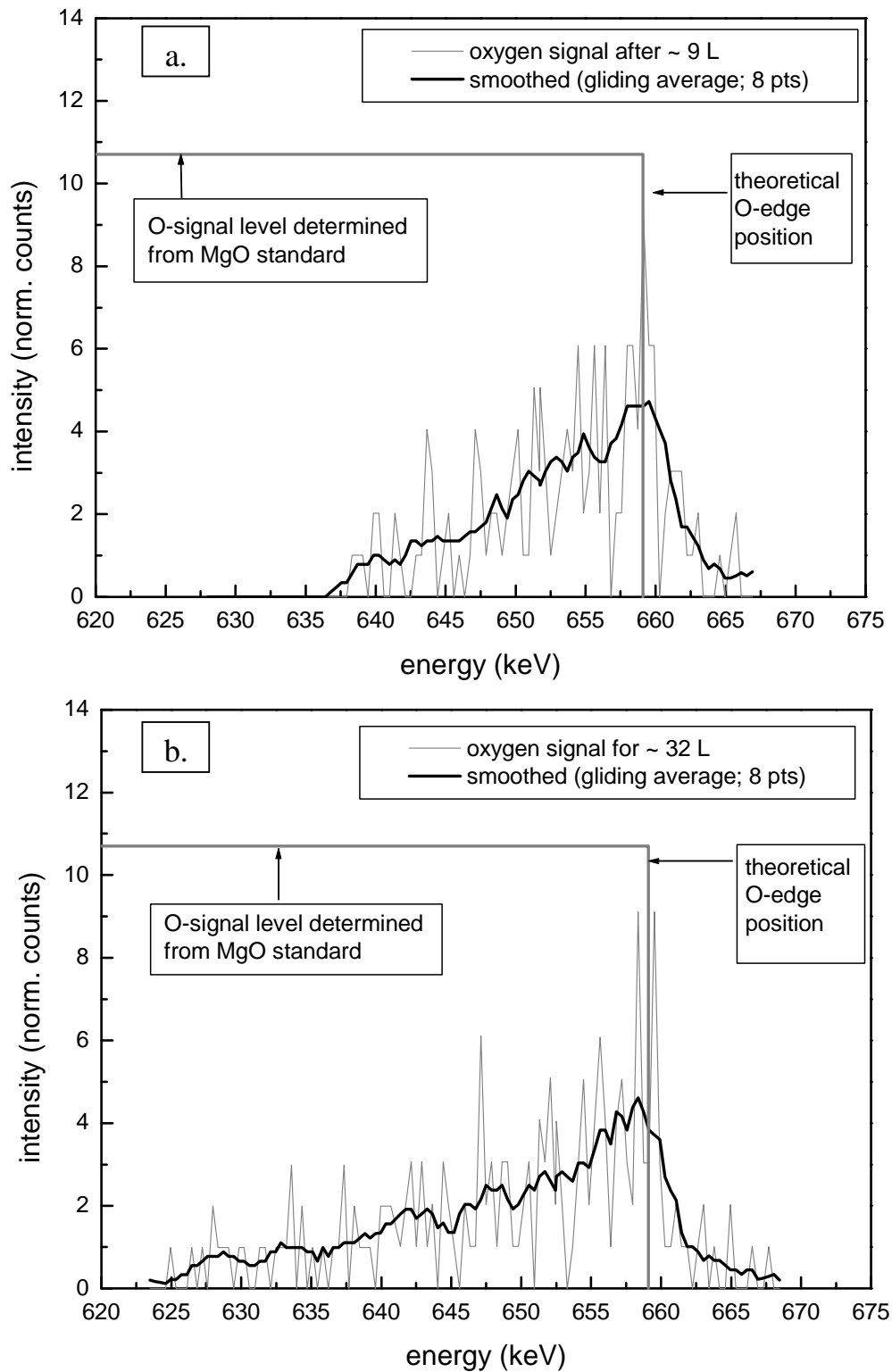


**Figure 4.14:** The O-signal as measured with HERDA for Mg samples oxidised with exposures of **a.** 9 L and **b.** 32 L of oxygen at room temperature and  $p_{\text{O}_2} = 1.3 \cdot 10^{-6}$  Pa. The signal level as measured from a MgO single crystal is also shown. The energy scale corresponds directly to a depth scale.

have a compensating charge corresponding to the local co-ordination of the oxygen ion. This result is compatible with the observation in the present work (see section 4.3) of a relatively large FWHM of the oxidic Mg XPS peaks indicating the existence of a large number of different oxidation states for Mg in the initial oxidation stage.

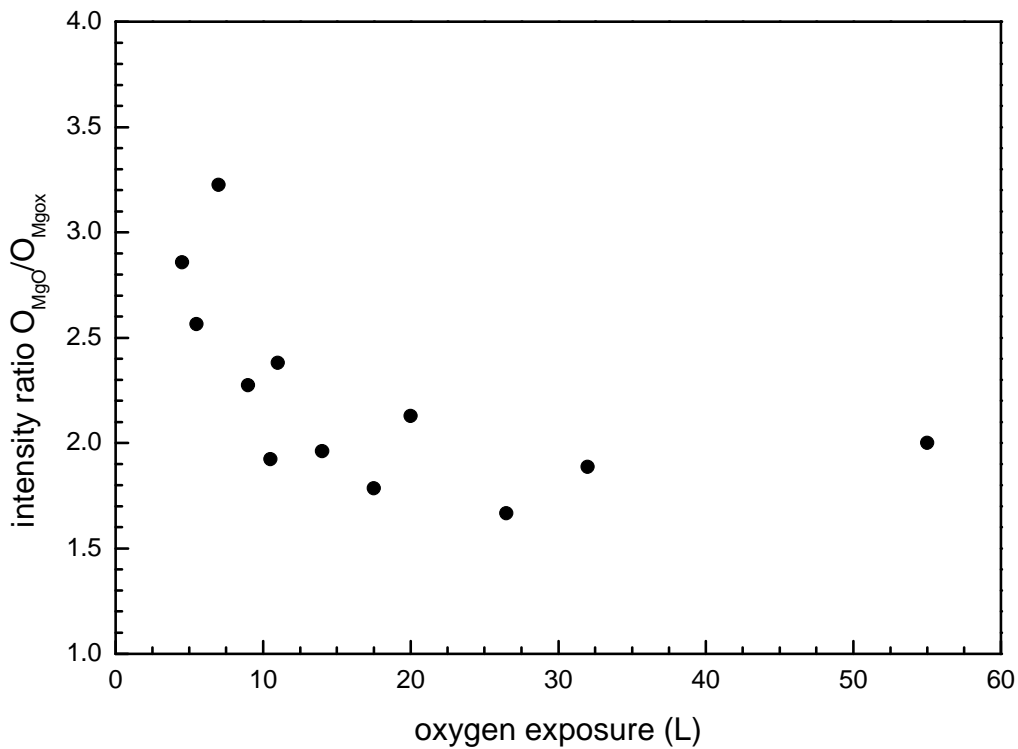


**Figure 4.15:** The HERDA intensity ratio of the oxygen signal due to MgO and the one due to the oxide built up after oxidation of Mg at room temperature as a function of oxygen exposure.

#### *Concentration gradient in the oxide layer*

Besides the Mg/O ratios determined from XPS measurements after each oxidation experiment in UHV, the Mg/O ratios as obtained upon a sputter depth profiling of the sample oxidised at 673 K and  $9.75 \cdot 10^4$  Pa in a separate furnace are shown as a function of (remaining) oxide thickness in Fig. 4.11. It follows, that a concentration profile occurs within the oxide layer, such that the Mg/O ratio increases from  $\sim 1.4$  at the surface to  $\sim 1.9$  at the metal-oxide interface. The dependence of the Mg/O ratio on oxide thickness as

determined by the sputter-depth profiling<sup>1</sup> coincides very well with the dependence of the Mg/O ratio on oxide thickness as determined by the measurements after each of the oxidation experiments in the UHV chamber. This implies that the composition of the initially formed oxide (at the substrate) does not change during oxidation and that new oxide with a lower Mg/O ratio is formed on top of the oxide already present.

The presence of a concentration gradient in the oxide layer, with increasing Mg/O ratio from the surface to the interface, is consistent with additional results obtained in this work. Determination of the Mg/O ratio of the oxide layers using the Mg 2p intensities yielded larger Mg/O values than by using the Mg 1s intensities. This can be explained by the considerably larger kinetic energy of the Mg 2p electrons as compared to the Mg 1s electrons, and the correspondingly larger information depth for the Mg 2p electrons. Thus, the Mg 2p peak contains a relatively large contribution of atomic layers close to the metal-oxide interface, where the higher Mg/O ratios occur (Fig. 4.11).

Further, the HERDA oxygen spectra exhibit a tail of decreasing intensity towards lower energies instead of a step function, as occurs for a homogeneous oxide layer (see Fig. 4.14). This observation is consistent with the presence of an oxide layer with a concentration gradient (increasing oxygen deficiency with increasing depth). The depth range over which the tail extends is larger than the thickness of the oxide layers as determined by XPS and ellipsometry. For 1.3 MeV Ar<sup>+</sup> ions, as used here, the effective stopping power in stoichiometric MgO is 8.62 keV/nm (section 4.3.3). On this basis the depths to which oxygen is observed would be about 3.7 nm for Fig. 4.14b and about 2.5 nm for Fig. 4.14a, which depth ranges are about two times larger than the layer thickness

---

<sup>1</sup> Because the composition-depth profile has been obtained by Ar<sup>+</sup> sputtering, it might be suggested that a changing Mg/O ratio upon sputter-depth profiling is caused by preferential sputtering. However, a significant effect of preferential sputtering is unlikely due to the relatively small difference in atomic weight of oxygen and magnesium atoms. Other authors have confirmed the absence of preferential sputtering in MgO [113]. Due to its relatively low kinetic energy and correspondingly lower concentration depth, the Mg 1s signal is more sensitive to the surface region of the specimen than the Mg 2p signal. Sputter depth profiling of bulk MgO showed a constant, slightly *larger* Mg/O ratio as derived from the Mg 1s signal (Mg/O = ~ 1.09) as compared to the Mg 2p signal (Mg/O = ~ 0.97). Hence, a minor effect of preferential sputtering cannot be excluded yet. However, note that this observation does not at all impede the conclusion that the oxide layers investigated possess an oxygen concentration gradient and exhibit a Mg/O ratio distinctly *larger* than that of MgO.

determined by XPS and ellipsometry in this work<sup>2</sup>. An explanation for this discrepancy could be that part of the oxygen is dissolved in Mg, which is not accounted for in the XPS

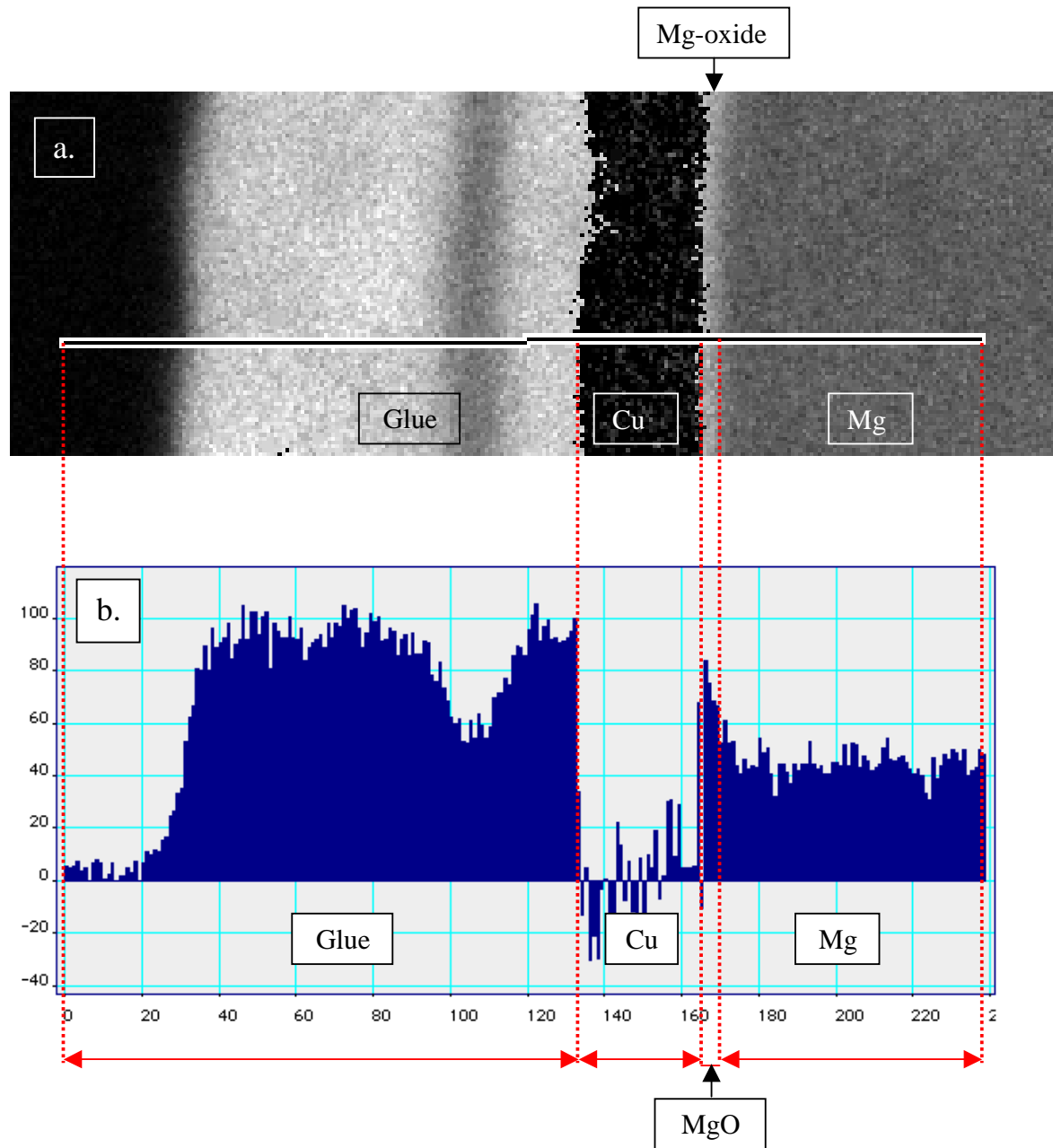


**Figure 4.16:** a. EELS map and b. EELS line profile taken from a. of a cross section of a Mg sample oxidised for 30 min at  $p_{O_2} = 1.3 \cdot 10^{-5}$  Pa. The position (abscissa) scale is in channels with 1 channel = 1.6 nm. (Measurements have been performed in a transmission electron microscope).

<sup>2</sup> Note that the results in Fig. 4.16 indicate the presence of an oxygen deficient Mg oxide, i.e. with a reduced density compared to MgO. Thus, the effective stopping power would be reduced, too, (in pure Mg metal it is  $\sim 4.2$  keV/nm) and the depth to which oxygen is observed would be even larger (7 to 8 nm).

analysis where it is assumed that the oxygen signal stems from oxygen only in the oxide layer (cf. section 4.3.1). This would only make the case for under-stoichiometric Mg-oxide formed in the initial oxidation stage even stronger.

The suggested presence of oxygen at depths as large as indicated by the HERDA data is supported by EELS measurements of a sample oxidised at room temperature for 30 min at  $p_{\text{O}_2} = 1.3 \cdot 10^{-5}$  Pa and sealed with a copper layer of 50 nm thickness, to protect against oxidation during cross section preparation. The EELS oxygen intensity of a part of the cross section of the sample is shown in Fig. 4.16. A line profile perpendicular to the oxide layer taken from Fig. 4.16a is shown in Fig. 4.16b. Apparently, the oxygen intensity at about the location where the oxide layer occurs extends over at least 7.5 nm, with the O concentration decreasing from the oxide surface with increasing depth.

Diffusion and dissolution of oxygen in the Mg substrate seems unlikely because of the low temperature applied and the very low solubility of oxygen in Mg (see Mg-O phase diagram in Ref. [114]). However, it may be suggested that in the first few nanometers of the (oxidised) Mg substrate equilibrium bulk thermodynamics do not hold (see also results for Al in [115]).

#### *Presence of OH in the oxide layer*

As mentioned in section 4.3.1 the O 1s spectra consist of two different peaks: one due to  $\text{O}^{2-}$  and one due to, most likely,  $\text{OH}^-$  signals (the origin of  $\text{OH}^-$  could be due to an H or  $\text{H}_2\text{O}$  contamination of the residual gas of the vacuum chamber and/or the oxygen gas). In the evaluation procedure the sum of the intensities of both peaks has been used for determination of the oxide composition (see above). The  $\text{OH}^-$  peak increases rapidly upon oxygen exposure and reaches a saturation value corresponding to about 25 % of the total area of the O 1s spectra (Fig. 4.17). From the sputter-depth profile of the samples oxidised at 673 K and at  $9.75 \cdot 10^4$  Pa a gradient of the hydroxide signal in the oxide layer could be determined. At the very surface of the oxide layer the hydroxide content is higher than near the metal substrate (Fig. 4.18), which agrees with results obtained for melt-spun Mg ribbons naturally oxidised in air for 7 years [35]. The temperature dependence of the hydroxide content is shown in Fig. 4.19. Evidently, below 400 K the hydroxide contribution is almost constant ( $\sim 30$  %) and for  $T > 400$  K the  $\text{OH}^-$  signal

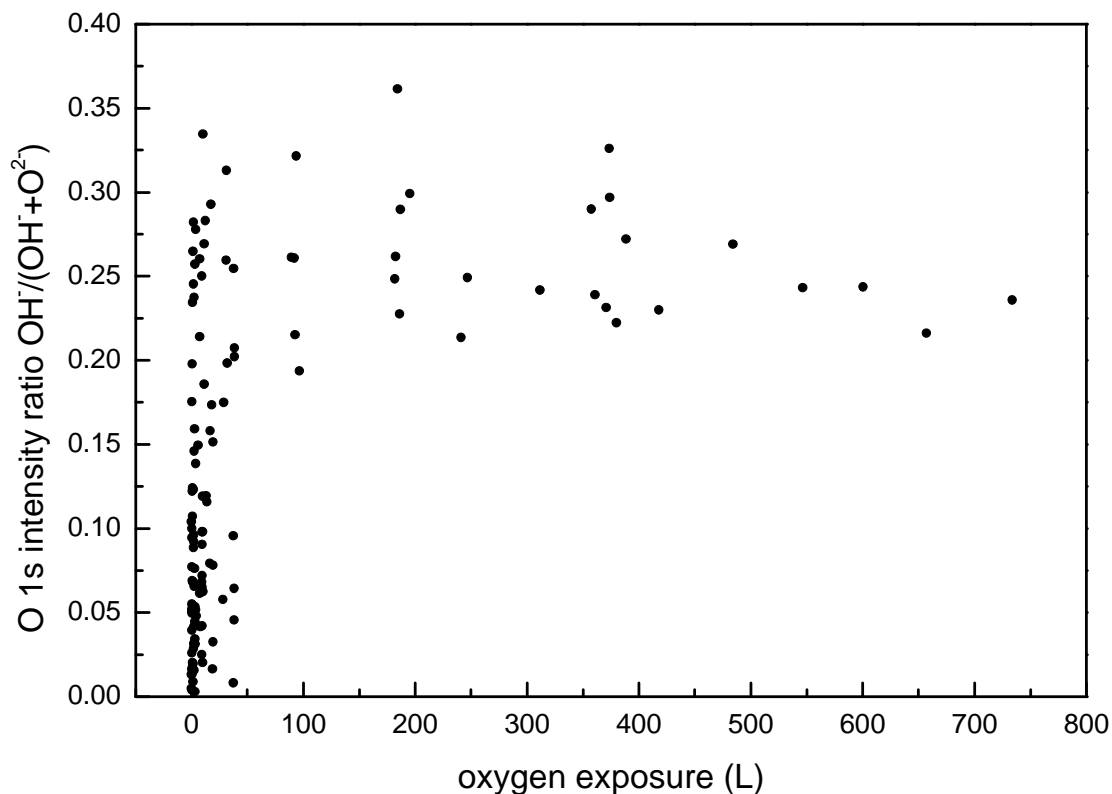


**Figure 4.17:** The high binding energy peak intensity, contained within the XPS O 1s signal and assigned to OH, relative to the total O1s intensity, as a function of oxygen exposure as derived from XPS data recorded for oxidation experiments performed at different temperatures and oxygen partial pressures in the UHV chamber.

distinctly decreases with increasing temperature.

Other interpretations of the high binding energy O 1s peak could be (i) the presence of dissolved oxygen within the metal substrate, which would support the interpretation of the HERDA results (see above), or (ii) the presence of chemisorbed oxygen on the surface of the oxide layer, which has been reported for the initial oxidation of magnesium [38,44]. However, both explanations are inconsistent with the results of the sputter-depth profile (Fig. 4.18): dissolved oxygen in the metal substrate should lead to an increase of the O 1s peak considered with decreasing thickness and chemisorbed oxygen should have disappeared after a few monolayers of oxide have been sputtered away, which both is not the case.

Since a second oxygen species is present, a contribution of this species (most likely a hydroxidic Mg component) in the Mg spectra may be present. However, as noted

in section 4.3.1, such a contribution, if present at all, could not be resolved (instrumental accuracy:  $\pm 0.1$  eV).

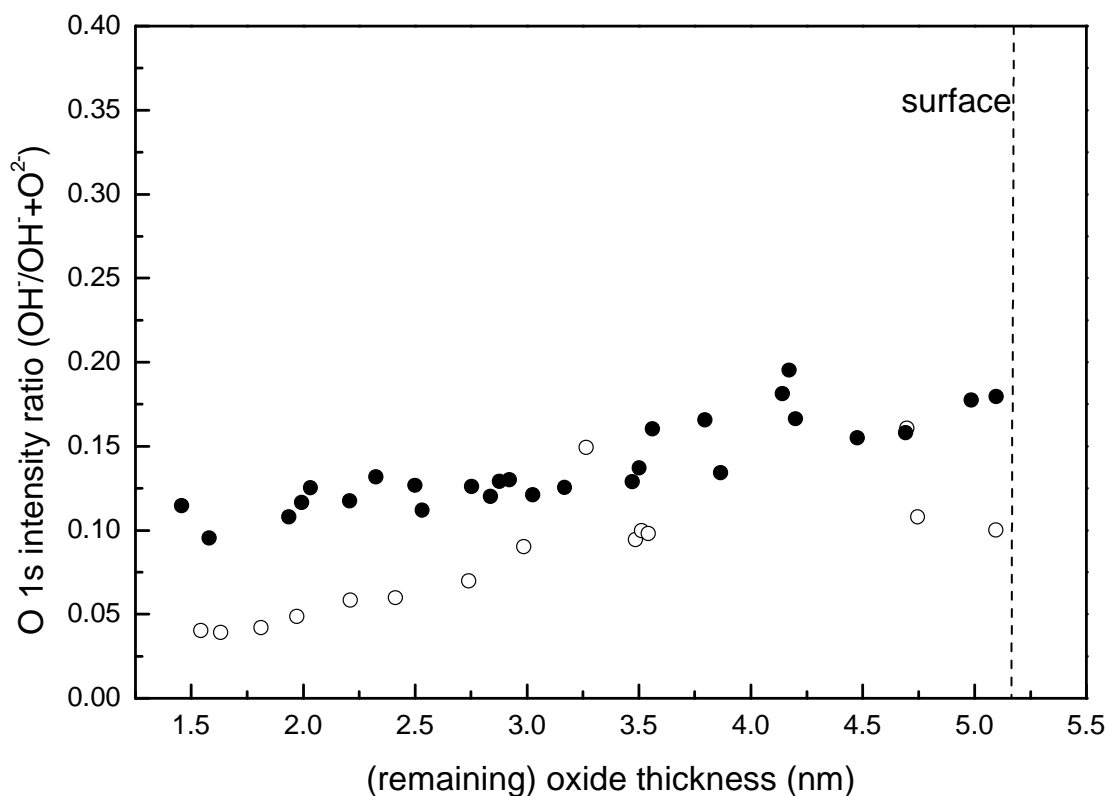


**Figure 4.18:** The high binding energy peak intensity, contained within the XPS O 1s signal and assigned to OH, relative to the total O 1s intensity, as a function of oxide thickness as determined from sputter-depth profiles measured by XPS after (separate) oxidation experiments at  $T = 673$  K and  $p_{O_2} = 9.75 \cdot 10^4$  Pa in a furnace. Filled and open symbols pertain to two different experiments.

#### 4.4.3 The oxidation state of magnesium; position and shape of the oxidic Mg 2p peak

##### *Position of oxidic Mg 2p peak*

The position of the Mg 2p peak of oxidic Mg relative to the position of metallic Mg (defined as the peak separation  $\Delta E_{sep}$ ) has been plotted versus oxide thickness in Fig. 4.20 for different oxygen partial pressures at 436 K. The relative position of the oxidic Mg 2p peak appears to be largely insensitive to the oxide thickness for each of the different oxygen partial pressures applied, but a clear decrease of the peak separation with increasing  $p_{O_2}$  can be recognised. The result for the sputter-depth profile of a sample

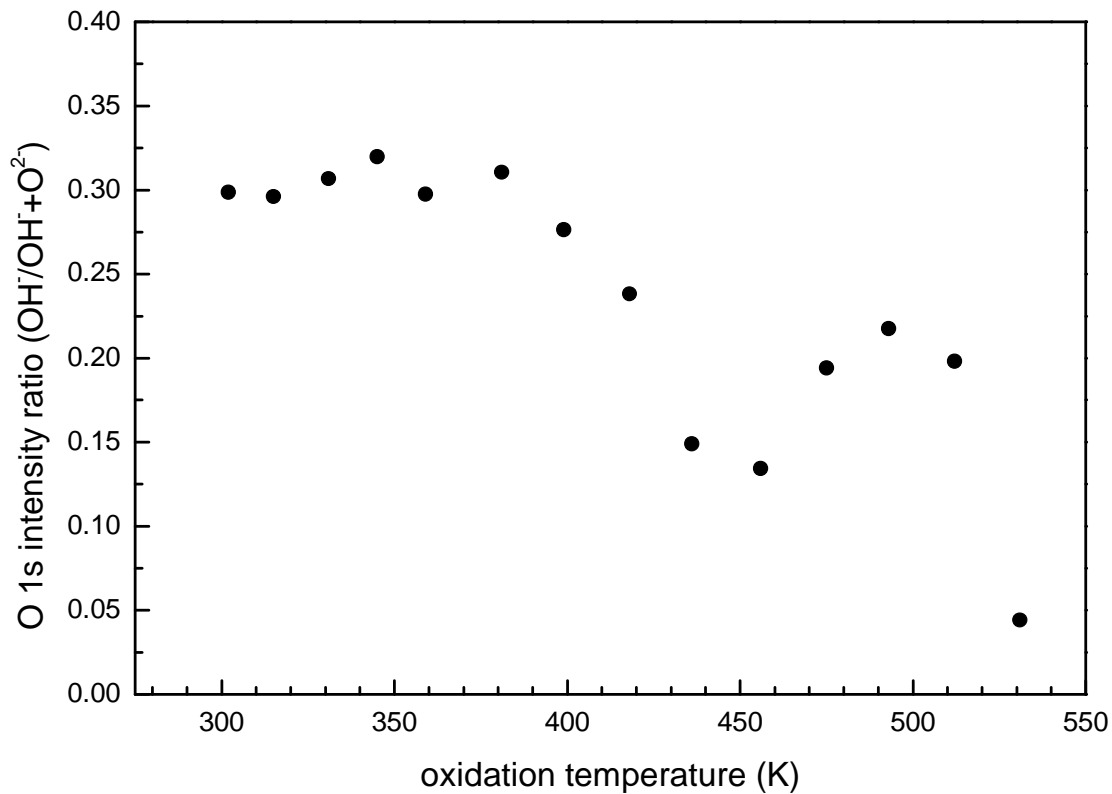


**Figure 4.19:** The high binding energy peak intensity, contained within the XPS O 1s signal and assigned to OH<sup>-</sup>, relative to the total O 1s intensity, as a function of oxidation temperature. All XPS measurements have been made after oxidation for 30 min at  $p_{O_2} = 1.3 \cdot 10^{-5}$  Pa.

oxidised at 673 K and  $9.75 \cdot 10^4$  Pa does reveal a gradient of  $\Delta E_{sep}$  within the oxide layer: A change (decrease) of  $\Delta E_{sep}$  by  $\sim 0.3$  eV going from the oxide surface to the metal substrate (Fig. 4.21).

The relative peak position of oxidic Mg for oxidation at constant time (30 min) and constant oxygen partial pressure ( $p_{O_2} = 1.3 \cdot 10^{-5}$  Pa) is shown as a function of temperature in Fig. 4.22. The peak separation increases from  $\sim 0.8$  eV to  $\sim 1.8$  eV with increasing temperature, reaching a saturation value of  $\sim 1.8$  eV at  $\sim 430$  K. Above 500 K  $\Delta E_{sep}$  starts to decrease. It can be concluded from Figs. 4.20 and 4.22 that  $\Delta E_{sep}$  is mainly influenced by  $p_{O_2}$  and T and much less dependent on oxidation time (oxide thickness).

Generally, the peak position of an oxidised metal relative to that of the pure metal can be explained with its oxidation state. If an isolated metal atom gets oxidised its

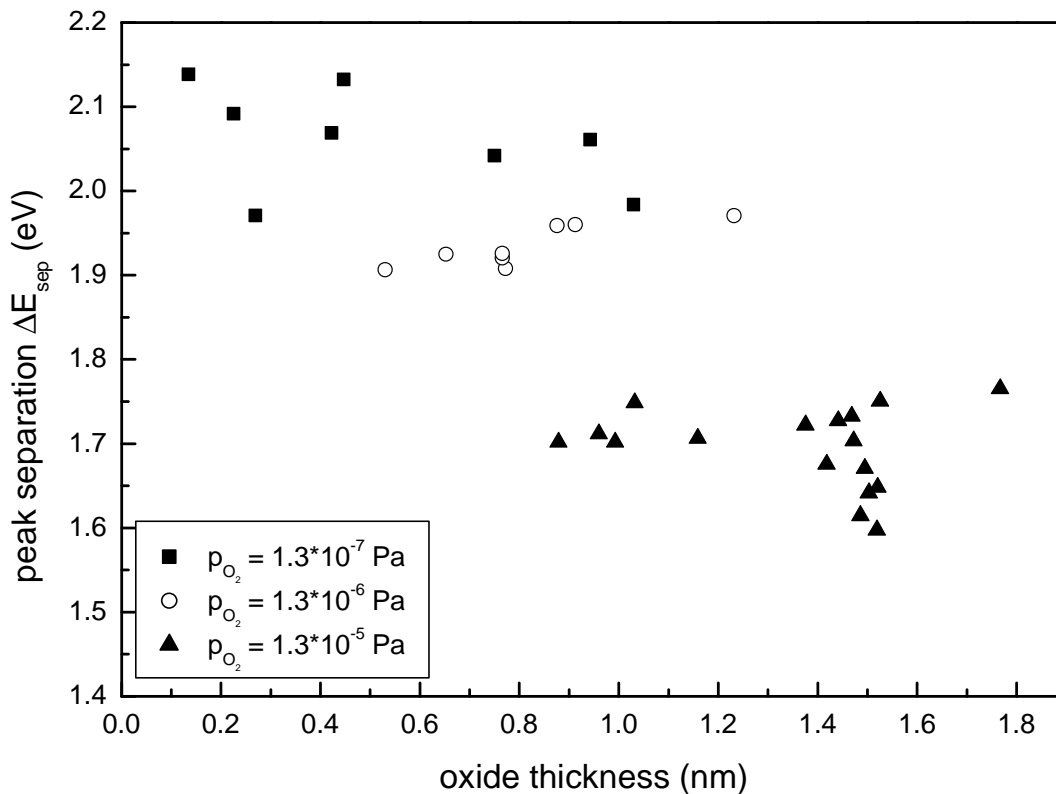


**Figure 4.20:** Difference in position between metallic and oxidic XPS Mg 2p peaks,  $\Delta E_{\text{sep}}$ , as a function of oxide thickness for specimens oxidised at oxygen partial pressures  $p_{\text{O}_2} = 1.3 \cdot 10^{-5}$ ,  $10^{-6}$  and  $10^{-7}$  Pa and at  $T = 436$  K.

valence electrons are pulled away from the atom. Thus the remaining core level electrons will be bound more strongly to the nucleus. The energies of core electrons are measured by XPS and therefore, most metals exhibit oxidic peaks shifted to higher binding energies (i.e.  $\Delta E_{\text{sep}} > 0$ ). Consequently, an *increase* of  $\Delta E_{\text{sep}}$  indicates that the valence electrons must have been pulled away *more strongly* from the metal atom. As soon as upon layer growth the oxide formed is the most stable oxide (stoichiometric MgO) the peak separation value should not change (increase) anymore. Thus, the observation of a (still) increasing peak separation indicates that the final oxidation state (assumed to be  $\text{Mg}^{2+}$ ) has not been reached yet. Hence, it would follow from the results presented (see Figs. 4.22 and 4.20) that the state of oxidation increases upon both increasing temperature and decreasing oxygen partial pressure. However, this interpretation seems incomplete:

- The highest oxidic Mg 2p binding energy is observed at the lowest partial pressures

(Fig. 4.20), where relatively thin oxide layers are formed with a composition far from MgO (see Fig. 4.11).

- A correlation between oxide composition and core-level binding energy would be expected, i.e. in the present case an increasing oxidic Mg 2p binding energy with decreasing Mg/O ratio (assuming that the oxidation state of oxygen is constant, namely -2, and that a charge neutral oxide film is formed). Such a correlation is not observed (compare Fig. 4.11 with Fig. 4.20).

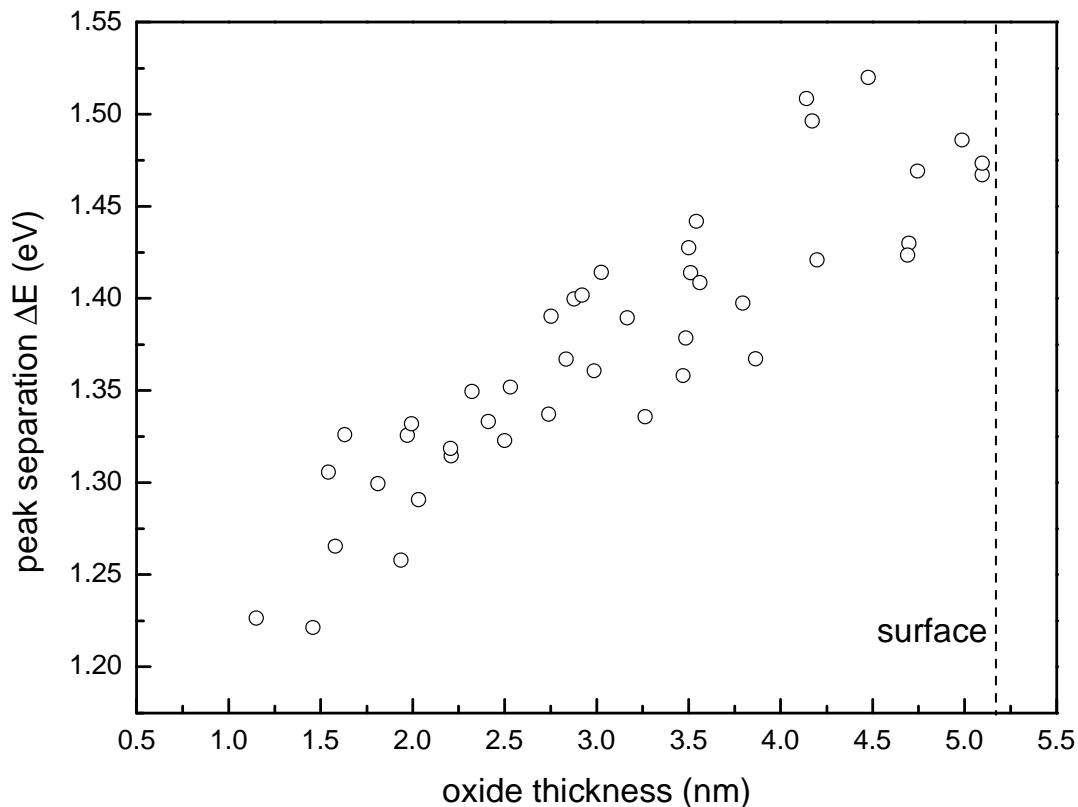


**Figure 4.21:** Difference in position between metallic and oxidic XPS Mg 2p peaks,  $\Delta E_{\text{sep}}$ , as a function of oxide thickness as derived from sputter-depth profiles of samples oxidised in a (separate) furnace at an oxygen partial pressure of  $p_{\text{O}_2} = 9.75 \cdot 10^4$  Pa and at  $T = 673$  K.

It is suggested that structure changes of the oxide may be responsible for the above indicated inconsistencies. For example the lower Mg 2p binding energy observed at the highest oxidation temperature (530 K) in Fig. 4.22 may be a consequence of a change of an amorphous to crystalline structure for the oxide, just above 500 K as supported by diffraction results reported in Ref. [32] (also for the samples oxidised at 673 K  $\Delta E_{\text{sep}}$

values distinctly smaller than 1.8 eV have been observed; see Fig. 4.21). Such a structural change from amorphous to crystalline depending on temperature, oxidation time and film thickness has also been reported recently for thin Al-oxide films [95,115-117].

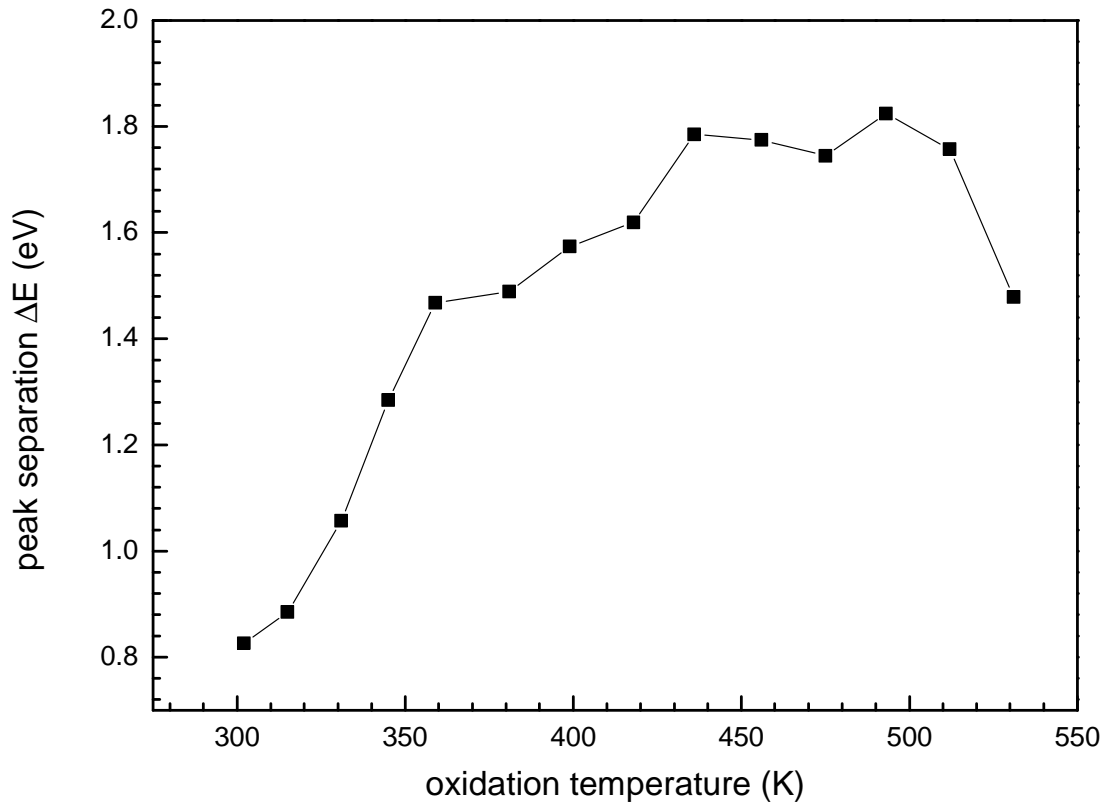


**Figure 4.22:** Difference in position between metallic and oxidic XPS Mg 2p peaks,  $\Delta E_{sep}$ , with temperature, for specimens oxidised for 30 min at  $p_{O_2} = 1.3 \cdot 10^{-5}$  Pa.

Note, that on the basis of literature data a difference in binding energy for the Mg 2p peak of metallic Mg and MgO of only 1.3 eV is expected (average value from the data in Ref.[118]), which is smaller than most of the values found in the present work (see Fig. 4.20). This is also an indication that the final oxidation stage (stoichiometric MgO) still has not been reached.

#### *FWHM of oxidic Mg 2p peak*

The full width at half maximum (FWHM) of the oxidic Mg 2p peak is shown as a function of oxide-layer thickness for the *in situ* oxidation experiments in Fig. 4.23 (see

open data points) for all oxidation temperatures and pressures investigated in the present work. The FWHM of the oxidic Mg2p peak decreases pronouncedly with increasing oxide thickness up to  $\sim 1.5$  nm. For very small oxide-layer thickness values a very large FWHM value occurs ( $\sim 3.5$  eV); but note uncertainties in the evaluation of the oxidic Mg 2p peak for very small oxide-layer thickness. For oxide thicknesses between 1.5 and 3.0 nm, the FWHM takes a minimum value of  $\sim 1.8$  eV. Above 3 nm the FWHM increases, which is possibly a consequence of the higher oxidation temperatures of the corresponding data points (see Fig. 4.24a). The results for the sputter-depth profile of the samples oxidised ex-situ at 673 K and at  $9.75 \cdot 10^4$  Pa have also been given in Fig. 4.23 (see filled data points). The FWHM decreases from the surface of the oxide in the direction of the metal-oxide interface. The results of the sputter-depth profile appear to confirm that a minimum of the FWHM occurs at a layer thickness around 2 nm.

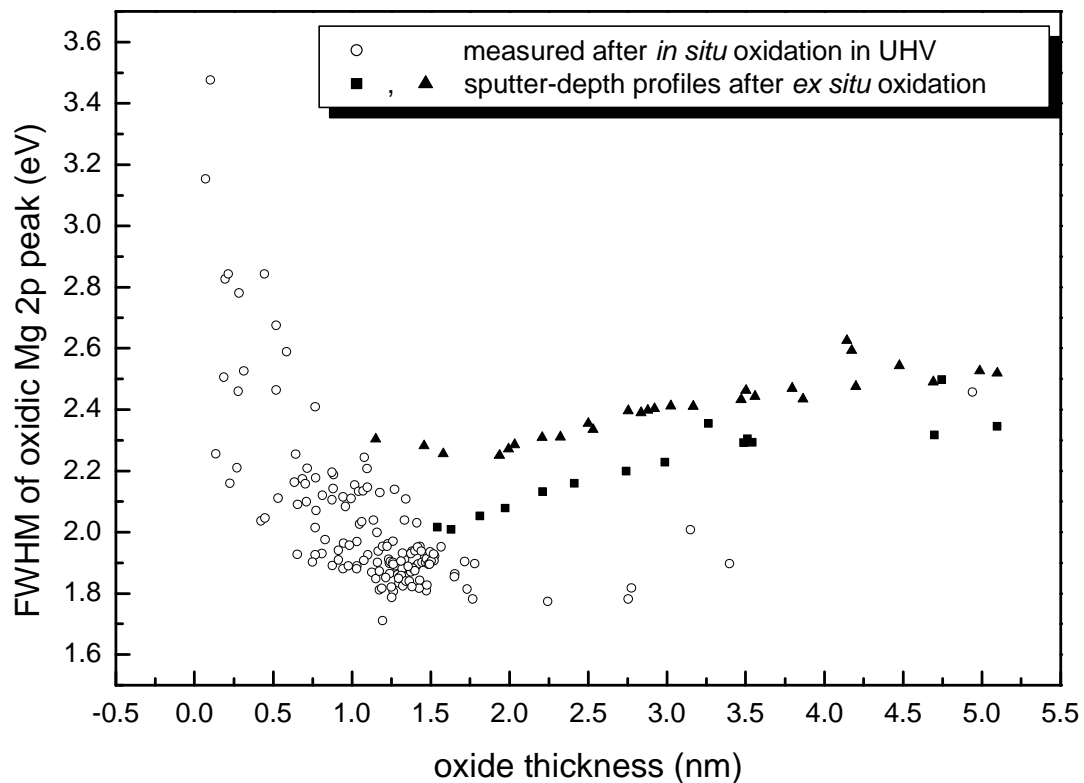


**Figure 4.23:** The full width at half maximum (FWHM) of the oxidic Mg 2p peak vs. oxide thickness. XPS data for all *in situ* oxidations (different temperature, oxygen partial pressure and oxidation time) in UHV, as well as from two sputter depth profiles recorded after *ex situ* oxidation at  $T = 673$  K and  $p_{O_2} = 9.75 \cdot 10^4$  Pa for 2 h in a (separate) furnace.

The temperature dependence of the FWHM is shown in Fig. 4.24 for oxidation at constant time (30min) and constant oxygen partial pressure ( $p_{O_2} = 1.3 \cdot 10^{-5}$  Pa). The FWHM is almost independent of temperature below  $\sim 450$  K. At higher temperature a strong increase of the FWHM occurs.

Generally, a change of the FWHM of the oxidic Mg peak can be explained by a change in the number of Mg oxidation states. The more oxidation states occur, the broader the peak is. Thus, the observation of a decreasing FWHM of the oxidic Mg 2p peak in the very initial stage of oxidation (Fig. 4.23) means that the number of Mg oxidation states is reduced upon growth of the oxide layer. This can be expected since the composition of oxide layer approaches the composition of MgO, containing only  $Mg^{2+}$ , with increasing layer thickness (Fig. 4.11). The increase of the FWHM for much larger oxide thicknesses (Fig. 4.23 and see at high temperatures in Fig. 4.24) may be related to structural changes in the oxide as discussed above for the oxidic-metallic peak separation.

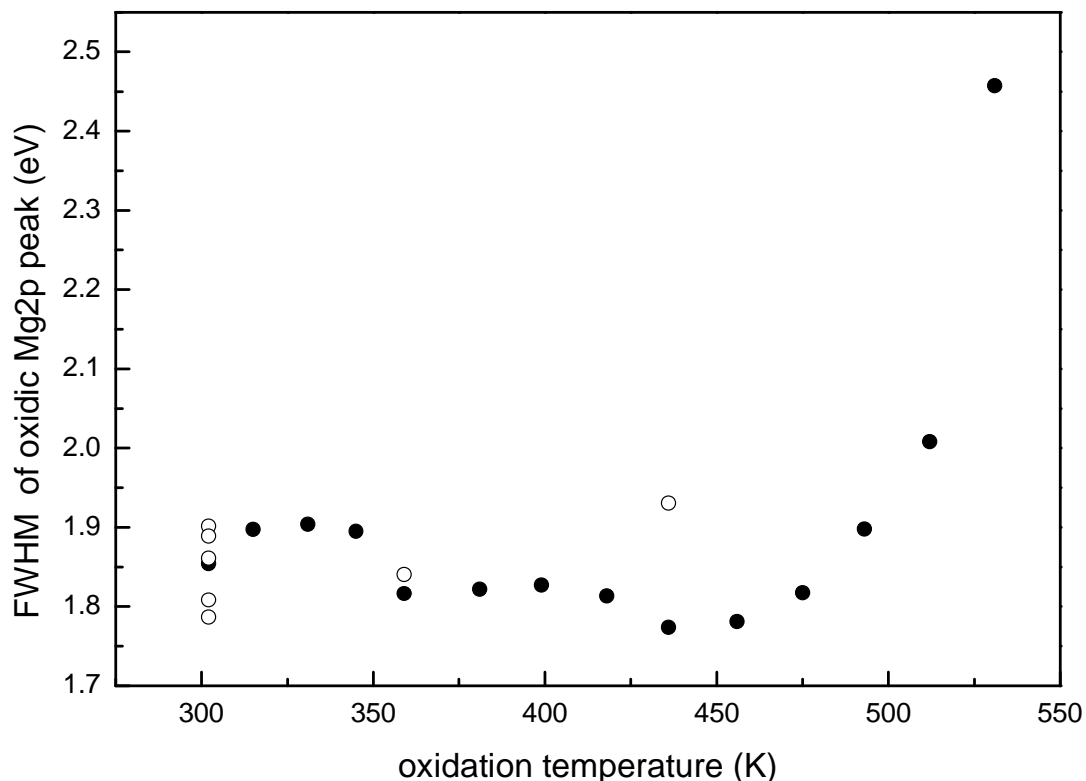


**Fig. 4.24:** The FWHM of the oxidic Mg 2p peak as a function of temperature for 30 min oxidations at  $p_{O_2} = 1.3 \cdot 10^{-5}$  Pa. Filled and open symbols represent two different measurement series.

#### 4.4.4. Band gap of the oxide

Pure, crystalline MgO is an isolator with a large band gap of 7.8 eV [83]. Thus, MgO is transparent for photons in the energy range covering both the visible and the near ultraviolet region (up to 7.8 eV). Therefore, the extinction coefficient  $k$  (cf. section 4.3.2) should be zero in the whole energy range covered by the ellipsometer used in this study (~1.5 eV to 5 eV; cf. section 4.2.4).

Following the evaluation procedure described in section 4.3.2, the optical constants  $n$  and  $k$  of the thin oxide layers on Mg formed after different oxidation times at 313 K and at an oxygen partial pressure of  $1.3 \cdot 10^{-6}$  Pa have been determined. The  $n$  and  $k$  values obtained in this way after long time (6900 s) oxidation, where the oxide layer composition is expected to lie within the saturation region, already, (cf. section 4.4.2), can be compared with the  $n$  and  $k$  values of pure MgO in Fig. 4.25. The  $n$  and  $k$  values of this oxide layer differ from those of bulk MgO, by the  $k$  values of the thin oxide layer being larger than zero for photon energies larger than about 2.5 eV. This indicates that the band gap of the oxide grown at this stage equals (only) 2.5 eV. Thin Mg-oxide films exhibiting relatively small band gap values and/or metallic conduction behaviour have been observed before [44,46].

The evolution of the band gap of the oxide layer with oxidation time at 313 K and at  $1.3 \cdot 10^{-6}$  Pa is shown in Fig. 4.26. It follows that in the very beginning of the oxidation process the band gap values are even lower than 2 eV. Furthermore, it should be recognised that due to the evaluation procedure, these band gap values are overestimated (see chapter 3.2), i.e. the true ones are probably (even) smaller. It might thus be that the band gap values are even equal to zero up to a certain oxide thickness. The experimentally determined development of the extinction coefficient  $k$  in the very early stages of the oxidation process is presented in Fig. 4.27. Upon ongoing oxidation the  $k$  values at the low photon energy side of the spectrum drop to zero. Up to about 30 s of oxidation  $k$  does not reach zero at any location in the energy range considered. Hence, in the very initial stage of oxidation the oxide layer possibly exhibits metallic-type conduction.

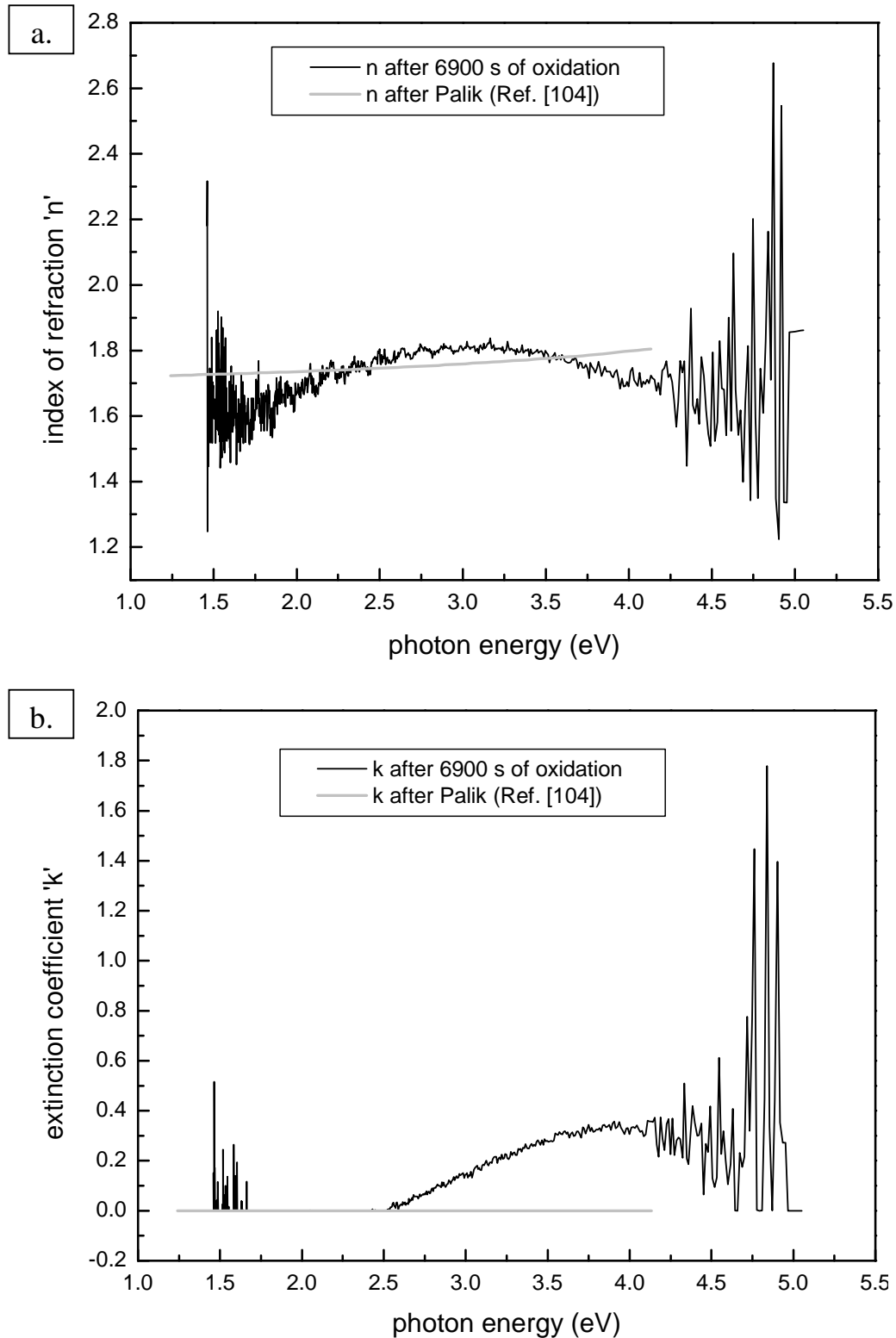


**Figure 4.25:** Comparison of **a.** the  $n$  and **b.** the  $k$  values after 6900 s of oxidation at  $T = 313$  K and  $p_{O_2} = 1.3 \cdot 10^{-6}$  Pa (this work) with the values for pure (bulk) MgO as recorded in Ref. [104]. Note the large scatter at both ends of the measured spectra.

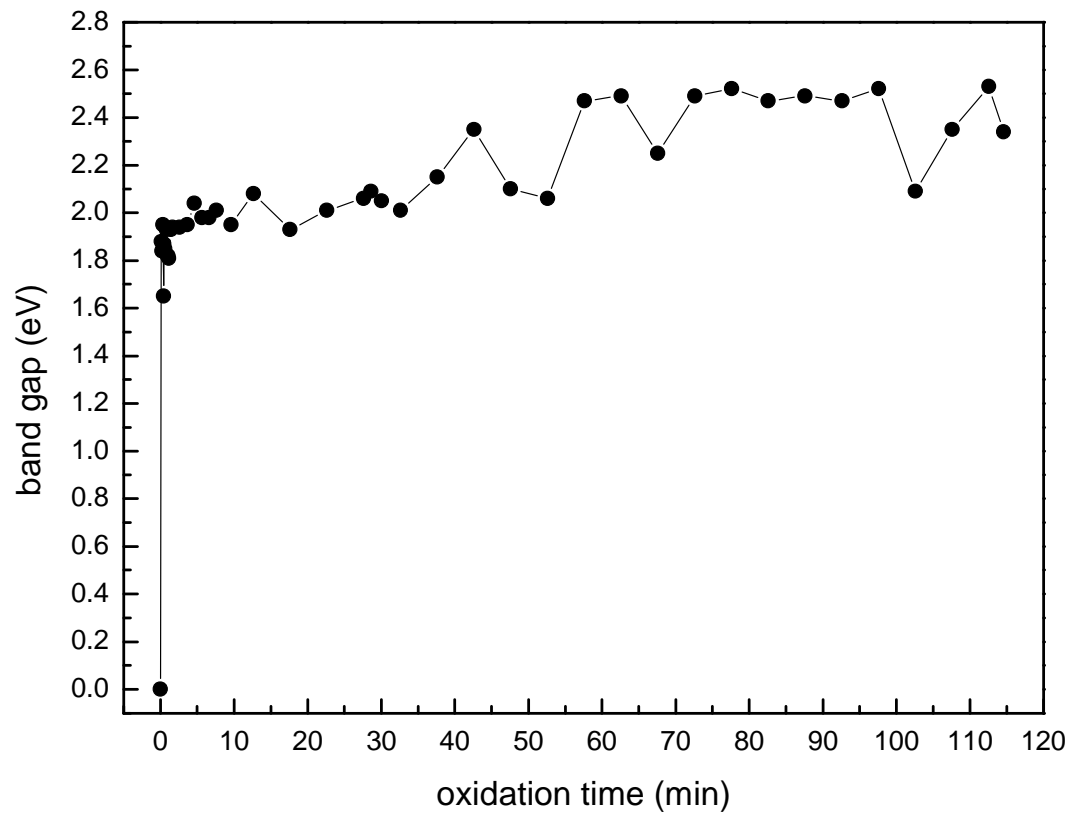


**Figure 4.26:** The band gap as a function of oxidation time as determined from the extinction coefficient as measured with ellipsometry for a sample oxidised at 313 K and  $p_{O_2} = 1.3 \cdot 10^{-6}$  Pa.

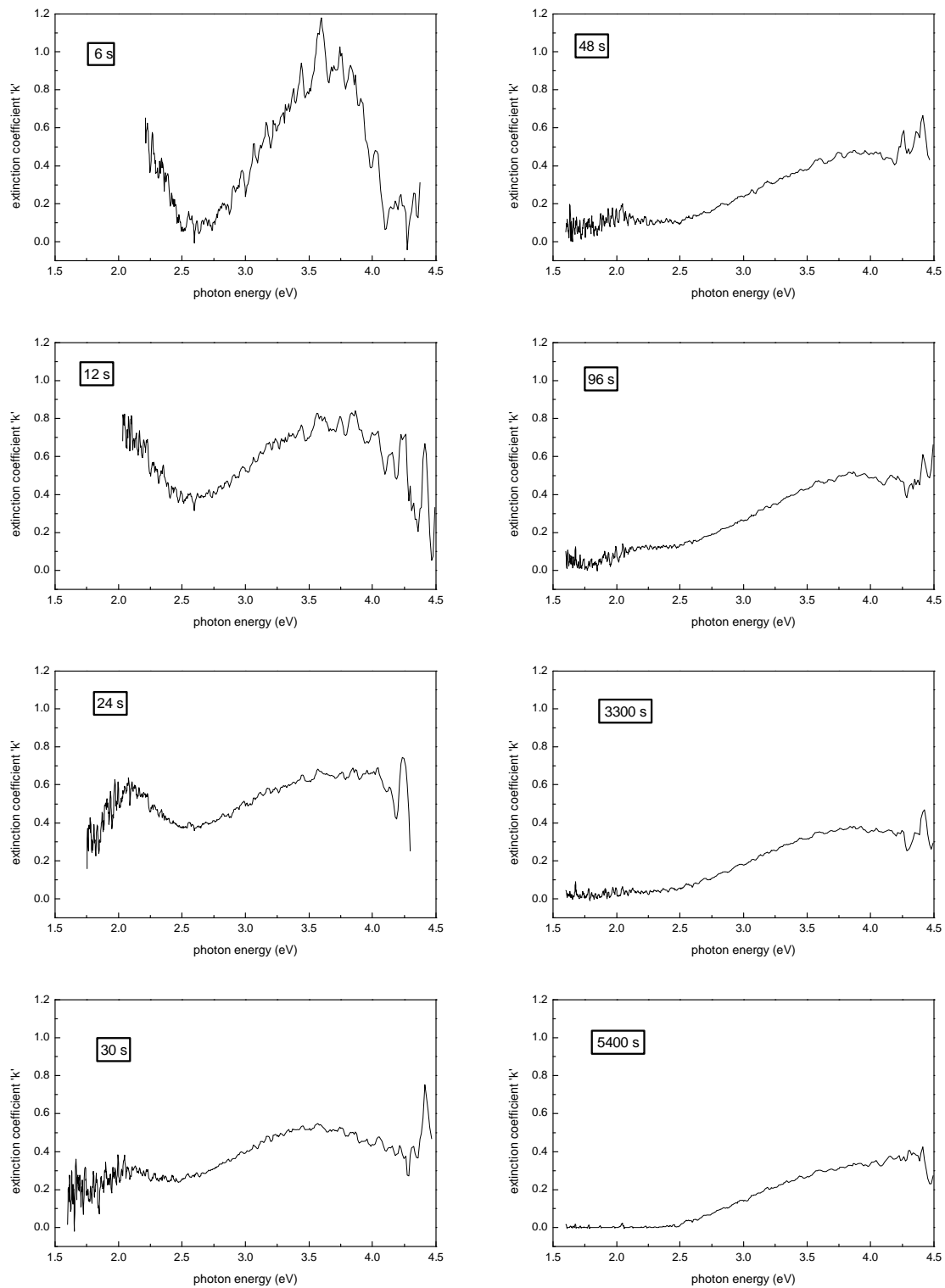


**Figure 4.27:** The extinction coefficient  $k$  as a function of photon energy for various oxidation times, as determined from ellipsometry measurements for a sample oxidised at 313 K and  $p_{O_2} = 1.3 \cdot 10^{-6}$  Pa.

## 4.5. Analysis of the oxidation kinetics

### 4.5.1. Theoretical background

After an isolating oxide film has formed on the substrate, the growth rate of the oxide-film is governed by the transport of cations (of Mg), anions (of O) and electrons through the layer. The most comprehensive model for such transport dominated oxide-film growth is due to Fromhold and Cook [84-86]. The approach departs from currents of cations/anions and electrons which are coupled by the constraint that no net electric charge is transported through the film. Until now this model has been applied to experimental data for only a few cases (example: initial oxidation of pure iron [87]). A concise summary of the model, as the outcome of a gradual development, has been presented recently [88]. The essential equations necessary for the specific analysis in this paper are listed with minimal comment below.

Absence of net electric charge transport through the film requires (i.e. coupled currents):

$$\sum_j q_j J_j = 0 \quad (4.18)$$

where  $J_j$  is the flux of species  $j$  with charge  $q_j$  through the film.

The relevant equation describing the thermally activated diffusion in an electric field for the ion (or ion-vacancy) current  $J_i$  is [87,88,119]:

$$J_i = 4av \exp\left(\frac{-W}{kT}\right) \sinh\left(\frac{Z_i e E_D a}{kT}\right) \frac{\left\{ C_i(D) - C_i(0) \exp\left(\frac{Z_i e E_D D(t)}{kT}\right) \right\}}{\left\{ 1 - \exp\left(\frac{Z_i e E_D D(t)}{kT}\right) \right\}} \quad (4.19)$$

with

$$E_D = -\frac{V_M}{D(t)} \quad \text{and} \quad V_M = \frac{1}{e}(\chi_0 - \chi_D) \quad (4.20a,b)$$

Here  $a$  is half the ionic jump distance,  $v$  is the ionic attempt frequency for jumping over the rate-limiting energy barrier  $W$ ,  $k$  is the Boltzmann constant,  $T$  is the absolute temperature,  $Z_i e$  is the effective charge per ion transported through the lattice ( $e$  is the magnitude of the electronic charge),  $E_D$  is the electric field in the oxide (see Eq. (4.20a)),

$V_M$  is the surface (Mott) potential (see Eq. (4.20b)),  $\chi_0$  and  $\chi_D$  are the metal-oxide work function and the oxide-oxygen work function, respectively,  $C_i(D)$  and  $C_i(O)$  are the defect concentrations of the diffusing ions at the oxide-oxygen interface and the metal-oxide interface, respectively and  $D(t)$  is the developing (time dependent) oxide film thickness.

The electronic tunnelling current  $J_e^{tunnel}$  is given by [84,88]:

$$J_e^{tunnel} = \frac{1}{8\pi^2 \hbar D(t)^2} \left[ \begin{array}{l} \{2\chi_0 + eE_D D(t)\} \exp\left\{-\frac{2\sqrt{m}D(t)}{\hbar} \sqrt{2\chi_0 + eE_D D(t)}\right\} \\ - \{2\chi_D - eE_D D(t)\} \exp\left\{-\frac{2\sqrt{m}D(t)}{\hbar} \sqrt{2\chi_D - eE_D D(t)}\right\} \end{array} \right] \quad (4.21)$$

Here,  $\hbar$  is Planck's constant  $h$  divided by  $2\pi$  and  $m$  is the effective electron mass.  $J_e^{tunnel}$  is the net electron flux due to tunnelling composed of a forward flux and reverse flux given by the two expressions within the large brackets of Eq. (4.21). Note that thermal emission (see Ref. [88]) is not considered here, since for the temperatures applied in the present work and the occurring oxide thicknesses (mostly  $< 2$  nm) the electron transport mechanism should be clearly governed by electron tunnelling [84,87].

#### 4.5.2. Fit procedure and results

The model described in section 4.5.1 has been fitted to the experimental data as follows.

- (i) The electric field strength,  $E_D$ , is calculated accounting to Eqs. (4.20 a and b) using the experimentally determined values  $D(t_i)$ , the constant parameter  $\chi_0$  and an starting value for the parameter  $\Delta X = \chi_0 - \chi_D$ , which in this step is a constant. Inserting  $E_D$  into Eqs. (4.19) and (4.21) both the cation flux and the electron tunnelling flux are calculated using a starting value for  $W$  and the values for  $a$ ,  $\nu$ ,  $C_i(O)$  and  $C_i(D)$  listed in Table 1 of Ref. [87]; deviating from [87], here  $Z = 2$  corresponding to  $Mg^{2+}$  and  $\chi_0 = 2$  eV have been used. The resulting net charge flux is determined and made zero according to the coupled-currents constraint (see Eq. (4.18)) by varying  $E_D$ . The value for  $E_D$ , for which the coupled-currents constraint is satisfied best (minimized) is returned.
- (ii) The resulting value for  $E_D$  is inserted into Eq. (4.19) yielding the cation flux  $J_{cat}(t_i)$  for the experimentally observed oxide thicknesses at time  $t_i$ .
- (iii) From the resulting value for  $J_{cat}$  at  $t = t_i$  the increment of time needed for layer

growth from  $D(t_i)$  to  $D(t_{i+1})$  can be assessed:

$$\Delta t_i \equiv t_{i+1} - t_i = \frac{D(t_{i+1}) - D(t_i)}{\Delta V_{ox} \cdot J_{cat}(t_i)} \quad (4.22)$$

with  $\Delta V_{ox}$  as the oxide volume increase per cation incorporated in the layer.

(iv) The squared difference between the thus calculated set of values  $\Delta t_i$  and the set of experimental values of  $\Delta t_i$  is determined. It gets minimised as well as possible with a non-linear minimisation routine implemented in Matlab [77] by varying the values for both  $W$  and  $\Delta X$  in successive iterations of steps (i) to (iv).<sup>3</sup>

As outcome of a systematic investigation performed here it followed that  $W$ ,  $\chi_0$ , and  $\chi_D$  are the most sensitive parameters out of the large number of parameters in Eqs. (4.19) to (4.21).  $\Delta X$  has been found to be more determinative for the quality of the fit than both the work functions individually (see also Ref. [87]). Thus,  $W$  and  $\Delta X$  have been chosen as the only fit parameters in the procedure described above. The Mg cations are considered to be the mobile ion species, i.e.  $Z = 2$  has been used in Eq. (4.19), whereas the larger O anions are considered to be immobile.

The procedure used here implies (obvious) continuous increase of the thickness values ( $\Delta t$  is always positive according to Eq. (4.22)). However, experimental scatter could cause occasionally that  $D(t_{i+1}) < D(t_i)$ . This problem has been remedied for the XPS data by applying the fitting to thickness data which are averages of the thickness values obtained from various experiments performed at identical T- and p-conditions. For the cases where this averaging was not sufficient, the mean value of both the time and the thickness of two successive data points were substituted.

For the (practically continuously recorded) ellipsometric data the average time and thickness values for thickness segments of almost constant length ( $\sim 0.03$  nm) were applied in the fitting, that is, each length segment corresponds to one time segment. Thereby, all data points in one length segment are replaced by one average data point. This procedure also limits the overrating of the weight of data points in the saturation region where the oxide thickness is almost constant since it reduces the number of data points contained in this region.

Data corresponding to oxide thicknesses lower than 0.3 nm have been left out from evaluation, since the oxide layer very likely would not be closed up to this mean oxide thickness (cf. section 4.4.1).

The results of fitting the model to the XPS data pertaining to oxidation at 302 K and at oxygen partial pressures  $1.3 \cdot 10^{-5}$  Pa,  $1.3 \cdot 10^{-6}$  Pa and  $1.3 \cdot 10^{-7}$  Pa are shown in Fig. 4.28a. Satisfying fits have been obtained. (It should be noted that the values for the oxidation series at  $1.3 \cdot 10^{-5}$  Pa might be less reliable, because the data treatment for the XPS data described on the previous page reduced the amount of data for this partial pressure to 4 points only). A judgement of the quality of the fit, in particular the remaining influence of the large weight of data within the saturation region, can be made by another fit which was performed with the squared difference values of calculated and measured oxidation times multiplied with a weighting factor given by the slope between two successive data points, which enhances the weight of the early data points. This results in a good fit of the steep increase at the beginning of the curve (see Fig. 4.28b), but leads to deviations in the saturation region. The resulting values for the fit parameters of both fits have been gathered for each of the oxygen partial pressures.

fitparameter	$p_{O_2} = 1.3 \cdot 10^{-7}$ Pa		$p_{O_2} = 1.3 \cdot 10^{-6}$ Pa		$p_{O_2} = 1.3 \cdot 10^{-5}$ Pa	
	not weighted	weighted	not weighted	weighted	not weighted	weighted
energy barrier $W$ (eV)	0.87	0.73	1.34	0.83	2.85	2.30
work function difference $\Delta X$ (eV)	- 0.29	- 0.06	- 1.53	- 0.36	- 5.61	- 4.14

Table 4.1: Resulting values for  $W$  and  $\Delta\chi$  as obtained by fitting the model as described in section 4.5.1 to the XPS data recorded for different  $p_{O_2}$ , with and without the use of a weighting factor in the fitting (cf. section 4.5.2).

The change of the values of the fit parameters  $W$  and  $\Delta\chi$  due to the application of the weighting factor indicates a dependence of the fit parameters on the oxidation stage. It

<sup>3</sup> Note, that the reason why  $\Delta X$  is varied in this fitting procedure by adjusting only  $\chi_D$ , and not  $\chi_0$ , is because  $\chi_D$  is expected to change more with ongoing oxidation.

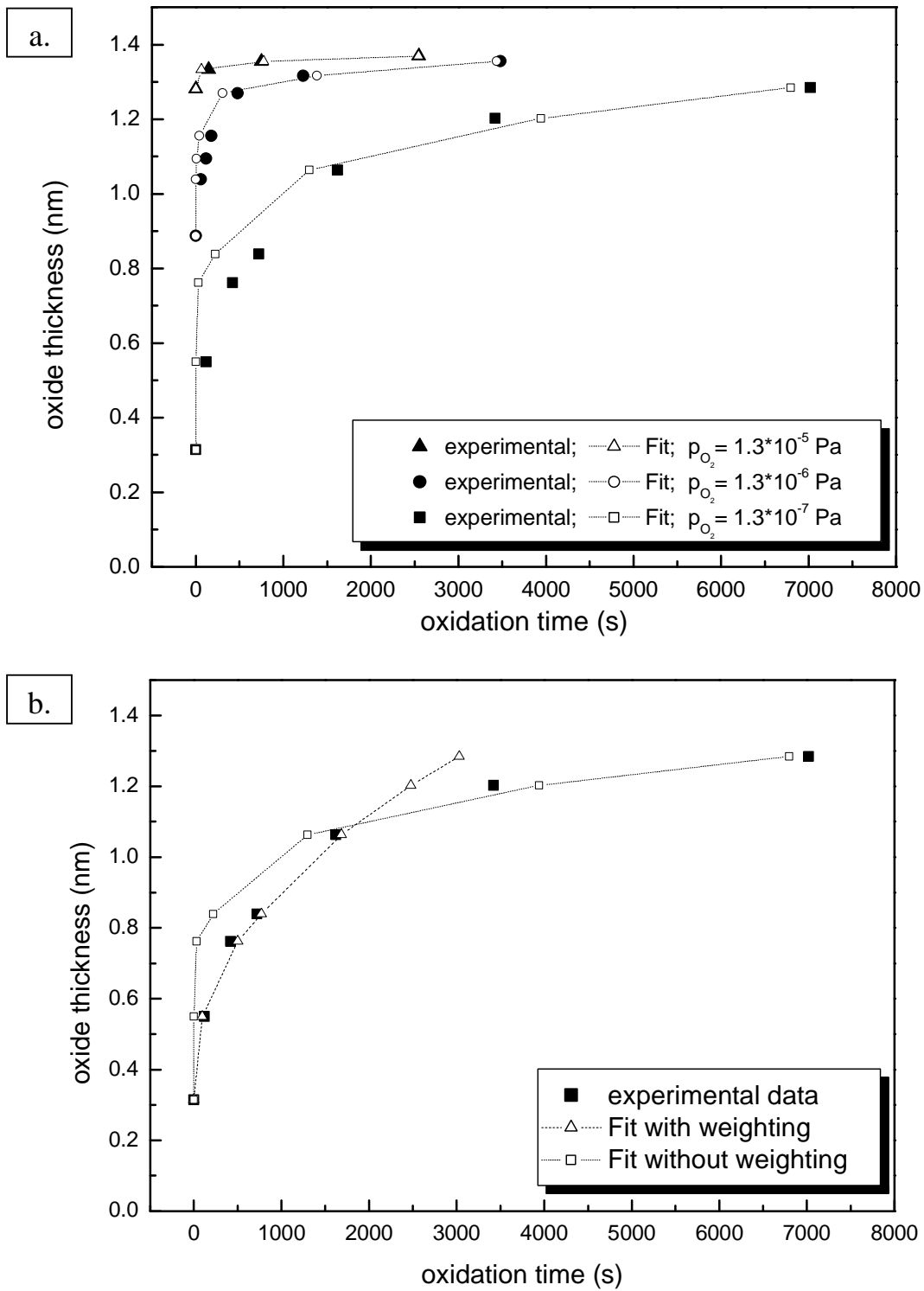


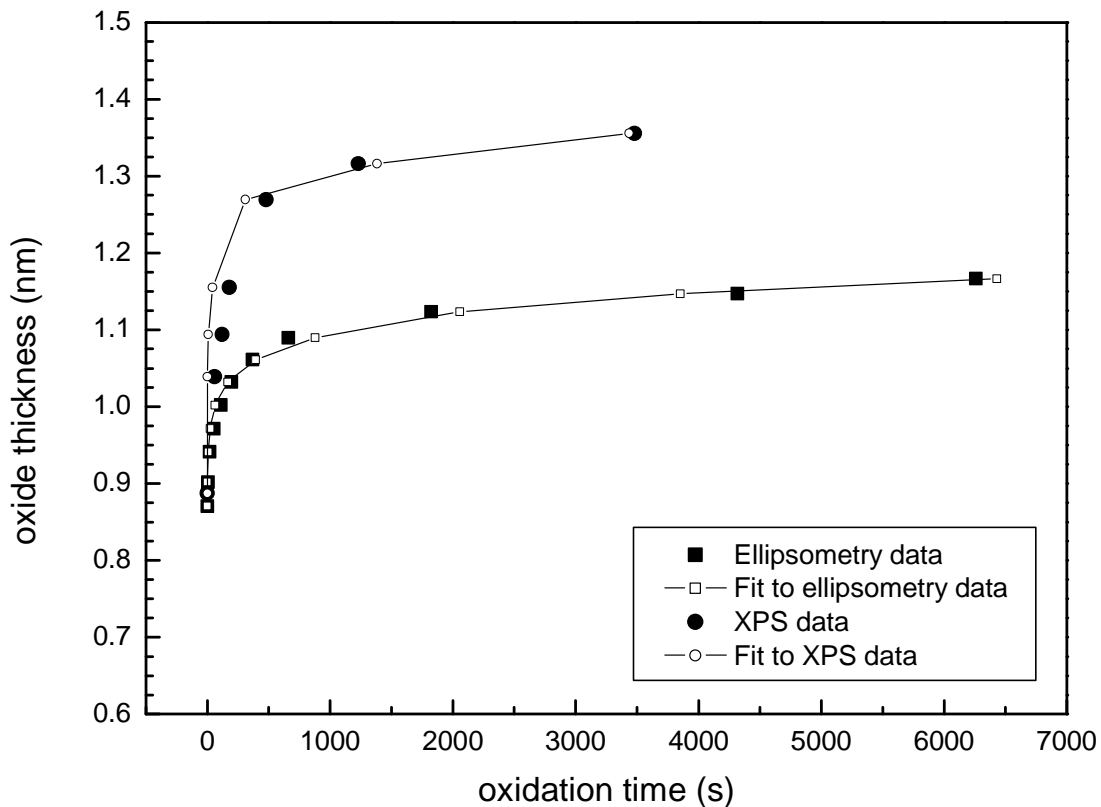
**Figure 4.28:** a. Oxide layer thickness vs. oxidation time for oxidations at 302 K and at three different oxygen partial pressures together with the results of the fit of the model described in section 4.5.1. b. Comparison of fit results with and without application of a weighting factor (cf. section 4.5.2) to the data from the oxidation experiments at 302 K and  $p_{O_2} = 1.3 \cdot 10^{-7}$  Pa.

has already been shown [87,120] that for the oxidation of iron and iron nitride a better fit could be obtained if  $\Delta\chi$  is taken time (or thickness) dependent (see also the evaluation below). Such a thickness/time dependence is probably due to the change of the composition of the oxide as shown in section 4.4.2 (cf. Fig. 4.11). The values determined for  $W$  and  $\Delta\chi$  show a distinct dependence on  $p_{O_2}$ . The model applied does not directly contain the oxygen partial pressure as a parameter (see section 4.5.1). However, the surface property  $\chi_D$  may depend on  $p_{O_2}$ . Thus, the change of  $\Delta\chi$  with  $p_{O_2}$  in Table 4.1 could be due to a  $p_{O_2}$  dependence of the oxygen-oxide work function  $\chi_D$ .  $W$  is not likely to be directly influenced by  $p_{O_2}$  as long as the same type of cation diffuses. But  $C_i(D)$  may depend on  $p_{O_2}$ , and because  $C_i(D)$  is taken as constant in the fitting, the values determined for  $\Delta\chi$  and  $W$  may indirectly depend on  $p_{O_2}$ . Or, the basic assumption, that film growth is rate controlled by the transport processes in the oxide film (see section 4.5.1), is violated.

Data sets acquired from XPS and ellipsometry measurements for the same oxygen partial pressure ( $p_{O_2} = 1.3 \cdot 10^{-6}$  Pa) and almost the same temperature (302 K and 313 K, respectively) are shown in Fig. 4.29, together with the model fits to those results. Since no XPS data below 0.8 nm are available (for the p- and T- conditions applied here) this range has been excluded from the fit for the ellipsometric data. Indeed, the resulting values for the parameters  $W$  and  $\Delta X$  are similar, as it should be (Table 4.2). The small differences are caused by the differences in thickness values of XPS and ellipsometry data, which are probably due to the neglect of elastic scattering of electrons in the XPS data evaluation and due to the use of different vacuum systems for the experiments as already discussed in section 4.4.1.

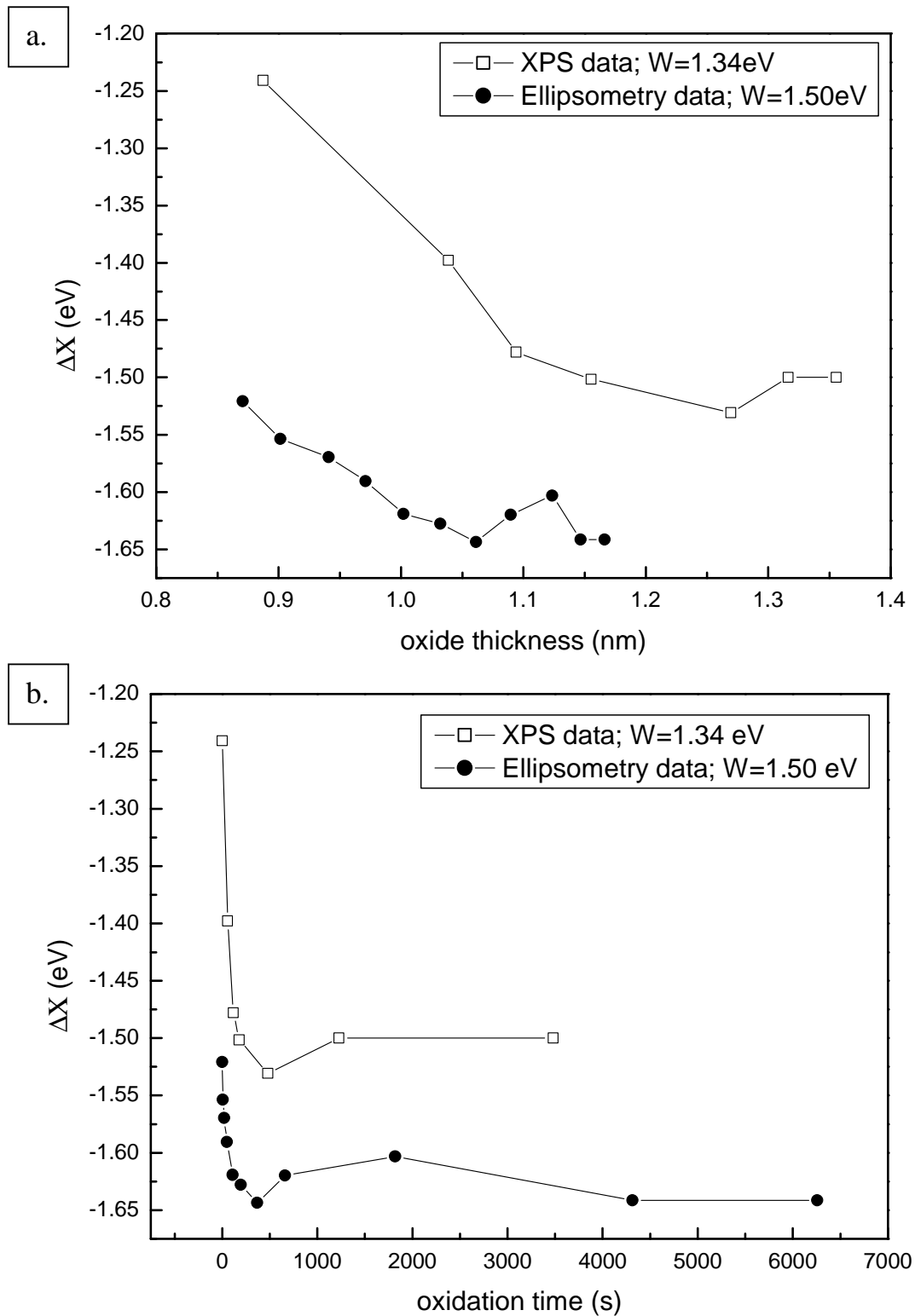
fit parameter	XPS data $p_{O_2} = 1.3 \cdot 10^{-6}$ Pa, T = 302 K	ellipsometry data $p_{O_2} = 1.3 \cdot 10^{-6}$ Pa, T = 313 K
energy barrier $W$ (eV)	1.34	1.50
work function difference $\Delta X$ (eV)	- 1.53	- 1.56

Table 4.2: Resulting values for  $W$  and  $\Delta\chi$  as obtained by fitting the model described in section 4.5.1 (without the use of a weighting factor; cf. section 4.5.2) to the XPS and ellipsometry data, separately, and as obtained for  $p_{O_2} = 1.3 \cdot 10^{-6}$  Pa using different UHV chambers.



**Figure 4.29:** Comparison of the fits of the model described in section 4.5.1 to ellipsometry data recorded from oxidation experiments at 313 K and  $p_{O_2} = 1.3 \cdot 10^{-6}$  Pa as well as to XPS data recorded from oxidation experiments at 302 K and  $p_{O_2} = 1.3 \cdot 10^{-6}$  Pa.

Taking  $W$  as a constant, i.e. independent of oxidation time (see discussion two paragraphs above) fits to the same experimental data can also be made adopting  $\Delta X$  as a time (thickness) dependent parameter. The value of  $W$  chosen has been taken from Table 4.2, i.e. 1.34 eV for the XPS data and 1.50 eV for the ellipsometry data. Note, that these values have been the outcome of the previously described fitting procedure using both  $\Delta X$  and  $W$  as fit parameters. The resulting change of  $\Delta X$  with oxide thickness (oxidation time) for both the XPS and ellipsometric data has been shown in Figs. 4.30 a and b. The work function difference  $\Delta X$  decreases with increasing oxide thickness and oxidation time, respectively, approaching a constant value for oxide thicknesses  $> \sim 1.1$  nm (corresponding to the ‘saturation’ thickness values in Fig. 4.7) and, at the p,T conditions applied, for oxidation times  $> 500$  s. The curve forms are similar for both the XPS and ellipsometry data. The quantitative differences might result from the slightly different



**Figure 4.30:** **a.** The work function difference  $\Delta X = \Delta\chi_0 - \Delta\chi_D$  vs. oxide thickness as determined from XPS and ellipsometry data recorded at  $T = 302\text{ K}$  and  $T = 313\text{ K}$ , respectively, and at  $p_{\text{O}_2} = 1.3 \cdot 10^{-6}\text{ Pa}$ .  $W$  has been taken constant ( $1.34\text{ eV}$  and  $1.50\text{ eV}$ , respectively). **b.** like **a.** but  $\Delta X$  plotted vs. oxidation time.

experimental conditions (oxidation temperatures are 302 K and 313 K, respectively) and from the use of a slightly different energy barrier  $W$  in the fitting procedure (see above).

#### **4.6. Summary**

Oxide growth on Mg is initiated by island growth. As determined from XPS measurements, up to a mean thickness of 0.5 nm the layer is not closed: at the surface oxide islands higher than 0.5 nm coexist with the bare metal possibly containing some incorporated oxygen below its surface (as indicated by HERDA and EELS measurements).

At temperatures up to 436 K and partial pressures of oxygen up to  $1.3 \cdot 10^{-5}$  Pa, the kinetics of oxide growth at constant temperature scales linearly with oxygen exposure, i.e. the product of oxidation time and the partial pressure of oxygen.

Within the first 2 to 4 L a rapid increase of film thickness takes place. Upon continued oxidation at temperatures up to about 440 K a saturation level for the thickness, 1.2 to 1.5 nm occurs. The occurrence of a 'limiting' thickness of the oxide film is due to the constraint of coupled currents of (Mg) cations and electrons due to tunnelling from the substrate, where the latter flux becomes negligibly small beyond the 'limiting' film thickness. Larger film thicknesses can be attained at higher oxidation temperatures (as observed in this study for temperatures  $> 440$  K; cf. Fig. 4.9) where thermal emission of electrons from the substrate becomes significant.

The model based on coupled cation transport and electron tunnelling provides a very good description of the observed oxidation kinetics (for both the XPS and the ellipsometric data). As a result, at constant temperature, a time-dependent difference,  $\Delta X$ , of the metal-oxide and oxide-oxygen work function is determined.

The initial oxide formed is strongly oxygen deficient as compared to MgO (derived from both XPS and HERDA measurements). In the beginning of the oxidation process each oxygen atom oxidises several Mg atoms. With ongoing oxidation, the composition approaches the stoichiometric value but is still oxygen deficient for the oxidation conditions applied. The oxide contains a considerable amount of hydroxide, in particular at its surface (indicated by the occurrence of two peaks in the O 1s XPS spectrum). The presence of an oxygen-concentration gradient in the oxide, consistent

with an increasing oxygen deficiency with increasing depth, was confirmed for oxide layers in the thickness range of 5.5 nm to 1 nm from sputter depth profiles. These observations indicate that the oxide grows outwardly, in agreement with the above model for oxide-film growth, revealing a changing oxide composition.

Changes of the binding energy of the Mg 2p electrons in the oxide (peak position and peak width in the XPS Mg 2p spectra) cannot only be explained with a change of the oxidation state of Mg, developing towards  $\text{Mg}^{2+}$  as in stoichiometric MgO. The change in the trend of the position and width of the oxidic Mg 2p peak for oxide thicknesses  $> 3$  nm and for temperatures  $> 500$  K indicate the occurrence of a structural change, for example from amorphous to crystalline oxide.

The band gap energy of the initial oxide formed is strongly reduced as compared to bulk, stoichiometric MgO, as shown by determination of the extinction coefficient from the ellipsometry measurements: After prolonged oxidation at low temperatures a band gap energy of about 2.5 eV occurs, instead of 7.8 eV as for bulk, stoichiometric MgO. In the very beginning of oxidation the band gap is certainly smaller than 2eV: the very initial oxide may exhibit metallic-type conductor behaviour.

## Appendix

The inelastic mean free IMFP of photoelectrons has been calculated after Ref. [65]:

$$\lambda = \frac{E_{kin}}{E_p^2 \cdot \left( \beta \cdot \ln(\gamma \cdot E_{kin}) - \frac{C}{E_{kin}} + \frac{D}{E_{kin}^2} \right)} \quad (4.23)$$

with

$$E_p = 28.8 \cdot \sqrt{U}; \quad U = \frac{N_V \cdot \rho}{M}; \quad \beta = -0.0216 + \frac{0.944}{\sqrt{E_p^2 + E_g^2}} + 7.39 \cdot 10^{-4} \cdot \rho;$$

$$\gamma = \frac{0.191}{\sqrt{\rho}}; \quad C = 1.97 - 0.91 \cdot U \quad \text{and} \quad D = 53.4 - 20.8 \cdot U$$

$E_{kin}$  is the kinetic energy of the photoelectrons considered (in eV),  $\rho$  is the density of the traversed medium (in g/cm<sup>3</sup>) with  $M$  as its molecular weight (in g/mole),  $N_V$  is the number of valence electrons per atom and  $E_g$  its band gap energy (in eV).

For the calculation of the IMFP in pure Mg the following values for the parameters have been used:  $N_{V,Mg} = 2$ ,  $\rho_{Mg} = 1.74$  g/cm<sup>3</sup>,  $M_{Mg} = 24.31$  g/mol and  $E_{g,Mg} = 0$  eV, yielding  $\lambda = 3.482$  nm for Mg 2p electrons and  $\lambda = 0.727$  nm for Mg 1s electrons.

For the calculation of the IMFP in magnesium oxide  $N_{V,ox}$  has been taken as  $(C_{Mg}^{ox}/C_O^{ox}) \cdot N_{V,Mg} + N_{V,O}$  with  $N_{V,Mg} = 2$  and  $N_{V,O} = 6$  (for definition of  $C_{Mg}^{ox}$  and  $C_O^{ox}$ , see section 4.3.1). The molecular weight  $M_{MgOx}$  has been calculated as  $(C_{Mg}^{ox}/C_O^{ox}) \cdot M_{Mg} + M_O$ , with  $M_{Mg} = 24.31$  g/mole and  $M_O = 16.00$  g/mole. In the first iteration (see section 4.3.1) of the calculation of the IMFPs the values for  $C_{Mg}^{ox}$  and  $C_O^{ox}$  have been taken as for stoichiometric MgO, i.e. 88.82 mol/dm<sup>3</sup>. In further iterations the values obtained from the Mg 2p (or Mg 1s) and O 1s peak intensities with Eqs. (4.6) and (4.7) have been used. The starting values for the IMFPs have thus been 2.785 nm (Mg 2p), 0.673 nm (Mg 1s) and 2.027 nm (O 1s). The density  $\rho_{MgOx} = 3.585$  g/cm<sup>3</sup> has been taken equal to the theoretical value for MgO. For the band gap  $E_{g,MgOx} = 0$  eV has been used. Although the band gap of bulk MgO is 7.8 eV [83], the results obtained in this work (see section 4.4) show that the

band gap energy for the very initial oxide layer on Mg is close(r) to 0 eV rather than equal to the value of bulk, stoichiometric MgO. Hence, the use of  $E_g = 0$  for the calculation of the IMFP of the oxide layer is more reasonable than the use of the value for bulk, stoichiometric MgO.